Modeling piecewise planar fault discontinuities without element-partitioning in 3D reservoir-geomechanical models

Chuanqi Liu[a], Jean H. Prévost[a], N. Sukumar[b]

[a]*Department of Civil and Environmental Engineering, Princeton University, Princeton, NJ 08544, USA*
[b]*Department of Civil and Environmental Engineering, University of California at Davis, Davis, CA 95616, USA*

Abstract

Using the extended finite element method, faults can be introduced into a three-dimensional reservoir-geomechanical model without meshing to assess the potential for fault reactivation associated with industrial activities such as disposal of CO_2 or fluid extraction. The residuals to the governing equations include basis functions formed from the enrichment functions for strong and weak discontinuities. The traditional spatial integration scheme is based on an algorithm that partitions each enriched element into a collection of sub-tetrahedra, which is time and storage intensive. To avoid element-partitioning, we adopt the homogeneous numerical integration scheme (referred as HNI hereafter) where the integration of homogeneous monomials over each polyhedron is converted into the integration of the same monomials over the one-dimensional edges of the polyhedron by using Stokes's theorem and Euler's homogeneous function theorem. The integrands for the strong and weak discontinuities are derived to implement the integration scheme in the three-dimensional reservoir-geomechanical model. An example of a jagged fault is

presented to reveal the advantages of HNI scheme over the standard element-partitioning approach. Several other examples that involve fluid flow, fault sliding and fault sliding triggered by injection pressure are also presented to demonstrate that accurate and efficient computations are realized by the new integration scheme.
Keywords: faults, X-FEM, reservoir-geomechanics, integration scheme

1. Introduction

Faults are geological entities of rock where relative displacement can occur in the plane of the fault. During industrial activities such as disposal of waste water or CO_2, fault slip may reactivate due to the changes in hydraulic pressures and deformations of the rock matrix. The motion of faults may threaten the stability of wells, even induce seismicity (Sminchak et al., 2001; Ellsworth, 2013; Kim, 2013). Therefore, accurate and efficient simulation techniques are required to assess the potential for fault reactivation. Prévost and Sukumar (2016) proposed a three-dimensional reservoir-geomechanical model with the extended finite element method (X-FEM).

In the X-FEM, the finite element approximation is enriched by additional functions through the notion of partition of unity (Melenk and Babuška, 1996). This advance leads to the modeling of arbitrary discontinuities independent of the mesh without requiring remeshing (Moës et al., 1999; Sukumar et al., 2000). The X-FEM greatly simplifies fault modeling, but there still remain challenges and improvements that need to be made (Sukumar et al., 2015). One particular issue is the spatial integration of discontinuous functions, for which various approaches have been proposed in the X-FEM.

A straightforward and widely used approach is to partition the two subdomains separated by the crack surface. Each part can be subdivided into triangles in two dimensions (Moës et al., 1999) or tetrahedra in three dimensions (Sukumar et al., 2000) by introducing a centroid to perform standard integration. However, the arbitrary intersection between the mesh and the discontinuity plane may generate quadrature subdomains of complex shape. This is particularly acute in three-dimensional problems that contain jagged faults, where quite sophisticated methodologies are required. Thus, element-partitioning can be time-consuming and need significant storage due to the presence of the complicated geometric structures.

In order to eliminate the need for domain partitioning for quadrature, Ventura (2006) replaced the discontinuous Heaviside enrichment function by equivalent polynomials. The integral of the equivalent polynomial over the entire element domain gives the exact value of the discontinuous function integrated on sub-cells. Thus, the equivalent polynomial method allows for standard Gauss quadrature in the element. However, the methodology requires the computation of the exact solution for a generic position of the discontinuity to derive the polynomial coefficients. For a hexahedron, the equivalent polynomial is an involved expression due to the complexity arising from the potential intersections between the base mesh and the discontinuity plane. In addition, Ventura's approach cannot handle "kinks" within the element - the edge in 2D or crack plane in 3D must fully cut the element.

Lasserre (1998) transformed the integration of homogeneous functions on convex polyhedra into line integrations over edges, applying Stokes's theorem

and using the property of homogeneous functions. Following Chin et al. (2017), we refer to this approach as the homogeneous numerical integration (HNI) method. Chin et al. (2015) showed that the HNI method is also applicable for nonconvex polyhedra, and presented the numerical integration scheme of homogeneous functions in polar coordinates. Chin et al. (2017) implemented the HNI method to integrate both discontinuous and weakly singular functions in the two-dimensional X-FEM. However, the performance of the HNI method for three-dimensional problems has not been assessed so far.

In this work, we focus on the exact integration of homogeneous functions and implement the HNI scheme in three-dimensional reservoir-geomechanical models. The strong displacement discontinuity and the strong and weak discontinuities of hydraulic pressure across the faults are considered. The rest of the paper is organized as follows. Section 2 presents the algorithm of the HNI method for three-dimensional problems. Section 3 details the procedure of implementing the HNI method in the three-dimensional reservoir-geomechanical model with the X-FEM. Some examples and results are presented in Section 4. We conclude with some final remarks in Section 5.

2. Algorithm for Homogeneous Numerical Integration

For the sake of completeness, here we briefly introduce the algorithm of the HNI, focusing on the integration of monomials over polyhedra. More details on the HNI can be found in Lasserre (1998) and Chin et al. (2015). In this section, matrices and vectors are in bold-faced, and ∇ refers to the spatial gradient operator.

According to the product rule and Gauss's divergence theorem, for a scalar-field f and a vector field $\boldsymbol{X}$, one obtains

$$\begin{aligned}\int_\Omega \nabla \cdot (\boldsymbol{X}(\boldsymbol{x}) f(\boldsymbol{x})) d\boldsymbol{x} &= \int_\Omega (\nabla \cdot \boldsymbol{X}(\boldsymbol{x})) f(\boldsymbol{x}) d\boldsymbol{x} + \int_\Omega \nabla f(\boldsymbol{x}) \cdot \boldsymbol{X}(\boldsymbol{x}) d\boldsymbol{x} \\ &= \int_{\partial\Omega} (\boldsymbol{n} \cdot \boldsymbol{X}(\boldsymbol{x})) f(\boldsymbol{x}) dA,\end{aligned} \tag{1}$$

where Ω is the 3D domain bounded by $\partial\Omega$, $\boldsymbol{x}$ is the spatial position vector, $\boldsymbol{n}$ is the unit outward normal vector to $\partial\Omega$ and dA is the differential area on $\partial\Omega$. Here, we focus on monomials of the type of $f(\boldsymbol{x}) = x^\alpha y^\beta z^\gamma$, where α, β, and γ are constants. Thus $f(\boldsymbol{x})$ is a homogeneous function satisfying the condition that $f(\lambda \boldsymbol{x}) = \lambda^q f(\boldsymbol{x})$ for real number $\lambda > 0$ with the degree of $q = \alpha + \beta + \gamma$. According to Euler's theorem, we then have

$$\boldsymbol{x} \cdot \nabla f(\boldsymbol{x}) = q f(\boldsymbol{x}). \tag{2}$$

Choosing $\boldsymbol{X}(\boldsymbol{x}) := \boldsymbol{x}$, and substituting (2) into (1), yields

$$\int_\Omega f(\boldsymbol{x}) d\boldsymbol{x} = \frac{1}{3+q} \int_{\partial\Omega} (\boldsymbol{x} \cdot \boldsymbol{n}) f(\boldsymbol{x}) dA, \tag{3}$$

where $\nabla \cdot \boldsymbol{x} = 3$. Thus, an integration over a three-dimensional domain is converted into the integration over its two-dimensional surface. In particular, if we only consider the integration over a polyhedron whose surfaces are polygons, the right-hand side of (3) can be transformed into the following expression:

$$\int_{\partial\Omega} (\boldsymbol{x} \cdot \boldsymbol{n}) f(\boldsymbol{x}) dA = \sum_{i=1}^{n} \frac{b_i}{||\boldsymbol{a}_i||} \int_{A_i} f(\boldsymbol{x}) dA, \tag{4}$$

where b_i and $\boldsymbol{a}_i$ are the specified scalar and vector representing the i-th polygon as $\boldsymbol{a}_i^{\mathrm{T}} \boldsymbol{x} - b_i = 0$. Note that the outward normal vector and surface area

of i-th polygon are $\boldsymbol{a}_i/||\boldsymbol{a}_i||$ and A_i, respectively. If $\boldsymbol{x}_0$ is an arbitrary point located on a specific surface A_i, for all $\boldsymbol{x} \in A_i$, $\boldsymbol{X} = \boldsymbol{x} - \boldsymbol{x}_0$ can be expressed using two orthonormal vectors $\boldsymbol{X} = c_1\boldsymbol{e}_1 + c_2\boldsymbol{e}_2$, where c_1 and c_2 are dimensionless coefficients. Thus, when restricted to the surface, we have $\nabla \cdot \boldsymbol{X} = 2$. Substituting $\boldsymbol{X} = \boldsymbol{x} - \boldsymbol{x}_0$ into (1) and setting $\Omega = A_i$, yields

$$\int_{A_i} f(\boldsymbol{x})dA = \frac{1}{2+q}\left[\sum_j \int_L (\boldsymbol{x} - \boldsymbol{x}_0)\cdot \boldsymbol{n}_{ij} f(\boldsymbol{x})dL + \int_{A_i} \nabla f(\boldsymbol{x})\cdot \boldsymbol{x}_0 dA\right], \quad (5)$$

where $\boldsymbol{n}_{ij}$ is the normal vector of the j-th line segment of i-th surface. The first term on the right side of (5) is the sum of integrals along line segments, and $(\boldsymbol{x} - \boldsymbol{x}_0)\cdot \boldsymbol{n}_{ij}$ is the algebraic distance from $\boldsymbol{x}_0$ to ij-th line. We can use Gauss quadrature to compute the line integrals. For a monomial up to degree q, an n-point Gauss quadrature rule on each boundary edge with $n \geq (q+1)/2$ suffices for exact integration. The integrand of the second term is a summation of homogeneous monomials in 3D. Hence, we can apply (5) recursively to compute this integral until $\nabla f(\boldsymbol{x})$ is zero.

Combining (3) and (5), the integration of monomials over polyhedra can be transformed into the integration over line segments, and some extra integrands may be introduced. The weight of integrand along line segments comes from (1) orientation of the plane; (2) orientation of the line; (3) degree of the integrand; (4) the gradient operator; and (5) location of a point lying on the surface. In the integration process, the polyhedron can be convex or nonconvex. The primary assumption is that the integrands are homogeneous, which is evident since the integrands are derived from the gradient operator of homogeneous monomials. In practice, we start from the monomial with the lowest

degree (i.e. constant 1 with degree 0) to avoid recursive calculations involving the gradient. For a trivariate polynomial with degree q, it can be shown that we need $(q+1)(q+2)(q+3)/6$ monomials to integrate the polynomial. Thus, it is a one-time cost upfront and much faster than starting from the highest degree.

3. Implementation of the HNI method in the 3D reservoir-geomechanical model with X-FEM

Since the HNI method can precisely compute the integrals over arbitrary polyhedra without element-partitioning, we implement the HNI method in the three-dimensional reservoir-geomechanical model with the X-FEM. The details of the reservoir-geomechanical model are illustrated in Prévost and Sukumar (2016). Here, we repeat the approximations of displacement and pressure with X-FEM. Then, we demonstrate that the representative integrands of the residuals of the governing equations are summations of homogeneous monomials, which are suitable for the HNI method. In terms of notation, we write matrices and vectors in their component forms, thus σ_{ij} is the Cauchy stress tensor and b_i represents the body force. The spatial gradient is denoted by a comma, for example, $\sigma_{ij,j}$ represents the spatial gradient of Cauchy stress. Einstein summation convention is also adopted. Superscript 's' denotes solid variables, and 'f' represents fluid variables. A superimposed dot indicates time derivative.

3.1. Faults modeling with the X-FEM

In the geomechanics module, we treat the fault as an internal displacement discontinuity that allows slipping to occur using a Mohr-Coulomb type criterion. For the strong displacement discontinuity, the Heaviside function is used

for the enrichment. The displacement approximation within element e is:

$$u_i^{(e)}(\boldsymbol{x}) = \sum_I N_I(\boldsymbol{x}) u_{iI} + \sum_I N_I(\boldsymbol{x}) H(\boldsymbol{x}) \hat{u}_{iI}, \tag{6}$$

where $N_I(\boldsymbol{x})$ is the standard finite element shape function of node I, $u_{iI} = u_i(\boldsymbol{x}_I)$ is the displacement vector at the point $\boldsymbol{x}_I$. $\hat{u}_{iI} = \hat{u}_i(\boldsymbol{x}_I)$ is the degree of freedom associated with Heaviside-enriched function, and

$$H(\boldsymbol{x}) = \begin{cases} 1 & \textbf{if} \quad d(\boldsymbol{x}) > 0 \\ -1 & \textbf{if} \quad d(\boldsymbol{x}) < 0 \end{cases} \tag{7}$$

is the generalized discontinuous Heaviside function, where $d(\boldsymbol{x})$ is the signed distance to a fault Γ^c.

For the reservoir, the fault is either an internal fluid flow conduit that permits fluid flow to occur within the fault as well as to enter or leave the fault or is a barrier to flow (sealing fault). For a sealing fault, a pressure discontinuity must occur across the fault and the Heaviside discontinuous function is used to model the strong discontinuity. The approximation within an element e for the strong pressure discontinuity is:

$$p^{f,(e)}(\boldsymbol{x}) = \sum_I N_I(\boldsymbol{x}) p_I^f + \sum_I N_I(\boldsymbol{x}) H(\boldsymbol{x}) \hat{p}_I^f, \tag{8}$$

and the gradient of pressure is:

$$p_{,i}^{f,(e)}(\boldsymbol{x}) = \sum_I N_{I,i}(\boldsymbol{x}) p_I^f + \sum_I N_{I,i}(\boldsymbol{x}) H(\boldsymbol{x}) \hat{p}_I^f, \tag{9}$$

where $\hat{p}_I^f$ is the additional pressure degree of freedom at node I. For a fluid flow conduit, one must use a continuous pressure function that permits a dis-

continuous normal pressure gradient across the fault and the absolute distance function is employed to model the weak discontinuity. The approximation within an element e for the weak pressure discontinuity is:

$$p^{f,(e)}(\boldsymbol{x}) = \sum_I N_I(\boldsymbol{x}) p_I^f + \sum_I N_I(\boldsymbol{x})\psi(\boldsymbol{x})\hat{\hat{p}}_I^f, \tag{10}$$

where $\hat{\hat{p}}_I^f$ is the enriched degree of freedom and $\psi(\boldsymbol{x})$ is the absolute distance function with a discontinuous normal derivative across the fault Γ^c, which is defined as:

$$\psi(\boldsymbol{x}) = \min_{\bar{\boldsymbol{x}}\in\Gamma^c} ||\boldsymbol{x} - \bar{\boldsymbol{x}}||, \tag{11}$$

where $||\cdot||$ is the norm of a vector. The gradient of the pressure is:

$$p_{,i}^{f,(e)}(\boldsymbol{x}) = \sum_I N_{I,i}(\boldsymbol{x}) p_I^f + \sum_I N_{I,i}(\boldsymbol{x})\psi(\boldsymbol{x})\hat{\hat{p}}_I^f + \sum_I N_I(\boldsymbol{x})\psi_{,i}(\boldsymbol{x})\hat{\hat{p}}_I^f. \tag{12}$$

For a planar fault, the equation of the fault plane can be expressed as:

$$g(\boldsymbol{x})|_{\boldsymbol{x}\in\Gamma^c} = n_x x + n_y y + n_z z - d = 0, \tag{13}$$

where n_x, n_y, n_z, d are constants with $n_x^2 + n_y^2 + n_z^2 = 1$, and the normal outward vector of the plane can be presented as $\boldsymbol{n} = (n_x, n_y, n_z)$. Then, the distance function from a point $\boldsymbol{x}$ to the plane becomes:

$$\psi(\boldsymbol{x}) = |n_x x + n_y y + n_z z - d|\,, \tag{14}$$

The gradient of $\psi(\boldsymbol{x})$ is:

$$\psi_{,i}(\boldsymbol{x}) = H(\boldsymbol{x}) n_i. \tag{15}$$

3.2. Residuals for the governing equations

The governing equations for the hydro-mechanical coupled model are momentum conservation of the mixture and pressure equation. The Galerkin weak forms of governing equations, written for node I in element e, are given as follows:

$$\int_{\Omega_e} \left(\sigma_{ij,j} + \rho g_i\right) \tilde{N}_I d\Omega = 0, \tag{16}$$

$$\int_{\Omega_e} \left(\frac{\dot{p}^f}{M} + q^f_{i,i} + b v^s_{j,j}\right) \tilde{N}_I d\Omega = 0, \tag{17}$$

where $\sigma_{ij} = \sigma'_{ij} - b p^f \delta_{ij}$ are the components of the total stress, σ'_{ij} are the components of the effective stress tensor of the solid, $b = 1 - (K^s/K_s)$ is the Biot's coefficient, K^s and K_s are the bulk moduli of solid skeleton and grain, respectively, p^f is the pressure of fluid, δ_{ij} is the Kronecker-delta function, $\rho = (1-\phi)\,\rho^s + \phi\rho^f$ is the density of mixture, ϕ is the porosity, ρ^f and ρ^s are density of fluid and solid, respectively, g_i is the acceleration due to gravity vector, $1/M = 1/N + \phi/K_f$ with $1/N = (b-\phi)/K_s$, K_f is the fluid bulk modulus, q^f_i is the Darcy flux obtained by the Darcy's law, v^s_j is the solid velocity vector, $\tilde{N}_I(\boldsymbol{x}) = N_I(\boldsymbol{x})$ for standard degrees of freedom, $\tilde{N}_I(\boldsymbol{x}) = N_I(\boldsymbol{x})H(\boldsymbol{x})$ for Heaviside-enriched degrees of freedom and $\tilde{N}_I(\boldsymbol{x}) = N_I(\boldsymbol{x})\psi(\boldsymbol{x})$ for absolute distance function enriched degrees of freedom.

After usual integration by parts and applying divergence theorem, we can

derive the residual for (16) as:

$$
\begin{aligned}
r_{iI} &= f_{iI}^{\text{ext}} - f_{iI}^{\text{int}} + f_{iI}^{\text{fault}}, \\
f_{iI}^{\text{ext}} &= \int_{\partial\Omega_e - \Gamma^c} n_j \sigma_{ij} \tilde{N}_I dA + \int_{\Omega_e} \rho g_i \tilde{N}_I d\Omega, \\
f_{iI}^{\text{fault}} &= \int_{\Gamma^c} n_j \sigma_{ij} \tilde{N}_I dA, \\
f_{iI}^{\text{int}} &= \int_{\Omega_e} \sigma_{ij}^{\prime(e)} \tilde{N}_{I,j} d\Omega - \int_{\Omega_e} b p^{f,(e)} \tilde{N}_{I,i} d\Omega,
\end{aligned}
\tag{18}
$$

where f_{iI}^{ext} represents the external force, f_{iI}^{int} represents the internal force, and f_{iI}^{fault} is the contribution of fault elements. The computation of external force is conventional and the residual contributions arising from fault elements result in surface integrals. Hence, we only demonstrate the procedure to integrate the internal force in the Eq. 18. Gauss-quadrature scheme is often used to integrate the internal force as:

$$
\int_{\Omega_e} \sigma_{ij} \tilde{N}_{I,j} d\Omega = \sum_{p=1}^{\text{N}_{\text{int}}} w_p \sigma_{ijp} \tilde{N}_{Ip,j} \Omega_p, \tag{19}
$$

where $w_p = w(\boldsymbol{x}_p)$ is the weight at the integration point $\boldsymbol{x}_p$, $\sigma_{ijp} = \sigma_{ij}(\boldsymbol{x}_p)$ are the components of the Cauchy stress tensor, N_{int} is the number of integration points, $\tilde{N}_{Ip,j} = \tilde{N}_{I,j}(\boldsymbol{x}_p)$ is the gradient of shape function at $\boldsymbol{x}_p$, and Ω_p is the volume associated with the point p. Note that $\tilde{N}_{Ip,j}$ is a discontinuous function if the element is cut by a fault and the volume integral requires special treatment above and below the fault. Therefore, a common procedure is to partition the element into several tetrahedra to determine the positions of quadrature points. This element-partitioning strategy introduces complicated geometric structures, particularly for the cases containing kinked or jagged

faults.

In this work, we compute the internal force using HNI scheme to eliminate the need for element-partitioning. Since the non-linear behavior of rock is dominated by the existence of faults, which are modeled by a Mohr-Coulomb criterion, we believe that the assumption of rock matrix as linearly elastic is acceptable to assess the potential of fault reactivation (Jing and Stephansson, 2007). For linearly elastic materials, σ'_{ij} is a linear function of the strain ε_{ij}:

$$\sigma'_{ij} = \lambda \varepsilon_{kk} \delta_{ij} + 2\mu \varepsilon_{ij}, \tag{20}$$

where λ and μ are Lamé coefficients. With the assumption of small strain, the strain field within the element is obtained from (6) as

$$\varepsilon_{ij}(\boldsymbol{x}) = \sum_I N_{I,j}(\boldsymbol{x}) \left[u_{iI} + H(\boldsymbol{x}) \hat{u}_{iI} \right]. \tag{21}$$

For the standard degrees of freedom, $\tilde{N}_I(\boldsymbol{x}) = N_I(\boldsymbol{x})$, considering equations (8), (21) and (20), the internal force can expand as follows:

$$\begin{aligned}
&\int_{\Omega_e} \sigma'^{(e)}_{ij} N_{I,j} d\Omega - \int_{\Omega_e} b p^{f,(e)} N_{I,i} d\Omega \\
&= \int_{\Omega_e^+} 2\mu \sum_J N_{J,j} N_{I,j}(\boldsymbol{x}) \left(u_{iJ} + \hat{u}_{iJ} \right) d\Omega + \int_{\Omega_e^+} \lambda \left[\sum_J N_{J,k} N_{I,i}(\boldsymbol{x}) \left(u_{kJ} + \hat{u}_{kJ} \right) \right] d\Omega \\
&+ \int_{\Omega_e^-} 2\mu \sum_J N_{J,j} N_{I,j}(\boldsymbol{x}) \left(u_{iJ} - \hat{u}_{iJ} \right) d\Omega + \int_{\Omega_e^-} \lambda \left[\sum_J N_{J,k} N_{I,i}(\boldsymbol{x}) \left(u_{kJ} - \hat{u}_{kJ} \right) \right] d\Omega \\
&- \int_{\Omega_e^+} b \sum_J N_J N_{I,i}(\boldsymbol{x}) \left(p^f_J + \hat{p}^f_J \right) d\Omega - \int_{\Omega_e^-} b \sum_J N_J N_{I,i}(\boldsymbol{x}) \left(p^f_J - \hat{p}^f_J \right) d\Omega,
\end{aligned} \tag{22}$$

where $\Omega_e = \Omega_e^+ \cup \Omega_e^-$, $\Omega_e = \Omega_e^+$ for $H(\boldsymbol{x}) > 0$ and $\Omega_e = \Omega_e^-$ for $H(\boldsymbol{x}) < 0$.

For the enriched degrees of freedom, $\tilde{N}_I(\boldsymbol{x}) = H(\boldsymbol{x})N_I(\boldsymbol{x})$, we have:

$$
\begin{aligned}
&\int_{\Omega_e} \sigma_{ij}^{\prime(e)} N_{I,j} H(\boldsymbol{x}) d\Omega - \int_{\Omega_e} b p^{f,(e)} N_{I,i} H(\boldsymbol{x}) d\Omega \\
&= \int_{\Omega_e^+} 2\mu \sum_J N_{J,j} N_{I,j}(\boldsymbol{x}) \left(u_{iJ} + \hat{u}_{iJ}\right) d\Omega + \int_{\Omega_e^+} \lambda \left[\sum_J N_{J,k} N_{I,i}(\boldsymbol{x}) \left(u_{kJ} + \hat{u}_{kJ}\right)\right] d\Omega \\
&+ \int_{\Omega_e^-} 2\mu \sum_J N_{J,j} N_{I,j}(\boldsymbol{x}) \left(\hat{u}_{iJ} - u_{iJ}\right) d\Omega + \int_{\Omega_e^-} \lambda \left[\sum_J N_{J,k} N_{I,i}(\boldsymbol{x}) \left(\hat{u}_{kJ} - u_{kJ}\right)\right] d\Omega \\
&- \int_{\Omega_e^+} b \sum_J N_J N_{I,i}(\boldsymbol{x}) \left(p_J^f + \hat{p}_J^f\right) d\Omega - \int_{\Omega_e^-} b \sum_J N_J N_{I,i}(\boldsymbol{x}) \left(\hat{p}_J^f - p_J^f\right) d\Omega.
\end{aligned}
\tag{23}
$$

Thus, we have derived the set of representative integrands for the residual of the solid equation as $F^{\mathrm{s}}_{\mathrm{strong}}(\boldsymbol{x}) = \{N_{I,i}N_{J,j}(\boldsymbol{x}),\, N_{I,i}N_J(\boldsymbol{x})\}$. Note that here the intact element Ω_e only need to be split into two sub-domains according to the discontinuity for the integration. For each subdomain, the integrand is a summation of homogeneous monomials, which are suitable for the HNI. The sets of representative integrands for strong and weak discontinuities of pressure can also be derived as $F^{\mathrm{f}}_{\mathrm{strong}}(\boldsymbol{x}) = \{N_{I,i}(\boldsymbol{x}),\, N_{I,i}N_{J,j}(\boldsymbol{x})\}$ and $F^{\mathrm{f}}_{\mathrm{weak}}(\boldsymbol{x}) = \{N_{I,i}(\boldsymbol{x}),\, N_I N_J(\boldsymbol{x}),\, N_I N_{J,i}(\boldsymbol{x}),\, N_{I,i}N_{J,j}(\boldsymbol{x}),\, N_I N_{J,i}\psi(\boldsymbol{x}),\, N_{I,i}N_{J,j}\psi(\boldsymbol{x}),\, N_{I,i}N_{J,j}\psi^2(\boldsymbol{x})\}$. Note that the uppercase I and J label the nodes and the lowercases i and j indicate the directions, with $i, j = 1, 2, 3$. It is well known that nodal shape functions in the parent coordinates are summations of monomials. If we consider an element with constant Jacobian in the isoparametric map, i.e. $J_{ij} = \frac{\partial x_i}{\partial \varepsilon_j}$ are constants, the integrals of representative integrands in $F^{\mathrm{s}}_{\mathrm{strong}}(\boldsymbol{x})$, $F^{\mathrm{f}}_{\mathrm{strong}}(\boldsymbol{x})$, and $F^{\mathrm{f}}_{\mathrm{weak}}(\boldsymbol{x})$ are transformed into integrals of summations of monomials in

the local coordinate system, for example,

$$\int_{\Omega^e} N_{I,i}(\boldsymbol{x}) d\Omega = \int_{\Omega^e} |\boldsymbol{J}| \frac{\partial N_I(\boldsymbol{\xi})}{\partial \xi_j} \frac{\partial \xi_j}{\partial x_i} d\xi d\eta d\zeta. \tag{24}$$

where $|\boldsymbol{J}|$ is the determinant of the Jacobian matrix which is a constant, and $\frac{\partial \xi_j}{\partial x_i}$ are components of the inverse of the Jacobian matrix which are also constants. Since structured hexahedral and unstructured tetrahedral meshes are with constant Jacobian in the isoparametric map, the HNI method is therefore applicable to most meshes used in practice.

4. Numerical examples

In this section, five benchmark problems are considered. To show the advantage of the HNI over the integration scheme with element-partitioning, the first problem reveals the versatility of the HNI method to model a jagged fault. The second example compares the results using different cubature schemes for fluid flow within a domain meshed by tetrahedra. As the third example, we present results for the fault treated as a weak discontinuity. The fourth problem shows the sliding of a kink fault with a low friction angle. Lastly, we present an example to demonstrate that injecting a fluid can reactive a stable fault.

4.1. Jagged fault

The striking feature of the HNI method is exact integration of homogeneous functions over convex and nonconvex polyhedra without the need for complicated algorithms to partition the element. To show the versatility of the HNI method, we study a problem with a jagged fault. As illustrated in

Fig. 1, the jagged fault is composed by n kinked faults that are averagely distributed in the cube of $20 \times 100 \times 1$ m^3. The rock permeability used is $k_{rock} = 3.33 \times 10^{-14}$m^2, and a uniform inflow fluid flux $q^f = 10^{-3}$m^3/s is prescribed on the top boundary. No flow is assumed to take place on all lateral boundaries, and a free-flow boundary is used at the bottom where the fluid pressure $p^f = 0$. The faults are assumed to be sealing faults and assigned a permeability $k_n = k_t = 10^{-4} k_{rock}$. The fluid density is 1000 kg/m^3, and the porosity is 0.3. The structured mesh consisting of $15 \times 15 \times 15 = 3375$ hexahedra are fixed for different n (here $n = 0, 2, 10$ and 20). For clarity, as shown in the Fig. 1, we view the sample along the y-axis.

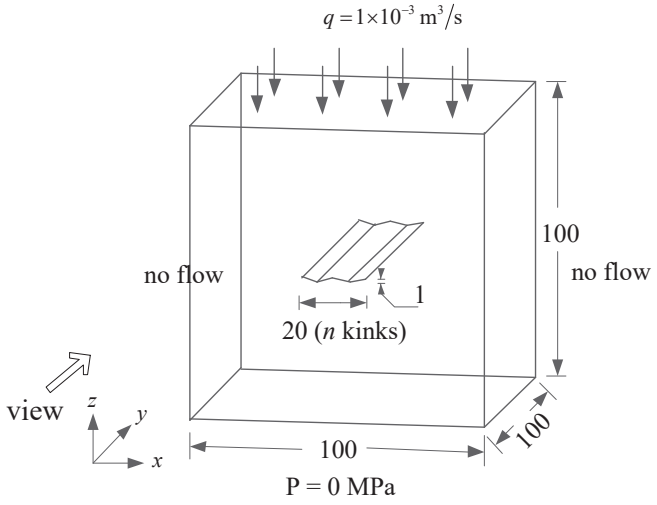

Figure 1: Geometry and boundary conditions for the case of a jagged fault (Unit: m)

Fig. 2 shows the distributions of excess pressure for different cases. The excess pressure is defined as $p^f_{\text{steady}} - p^f_0$, where p^f_{steady} is the fluid pressure in the steady state considering the fault and p^f_0 is the initial pressure in the continuum domain without the fault. The insets on the bottom-right of each

subfigure show the intersections of the fault and the central element. Since the fault acts as a barrier to flow, there is no fluid flow in the region below the fault resulting in the negative excess pressure. The maximum excess pressures for $n = 0$ and $n = 2$ are close, so as for $n = 10$ and $n = 20$. But the maximum pressure for $n = 10$ is one order of magnitude less than that for $n = 0$. From this example, we can see that the HNI method can handle the 3D jagged fault since only two polyhedra that are split by the fault are needed, whereas if we employed the integration scheme with element-partitioning, sophisticated algorithms and data structures would be needed for the partitioning.

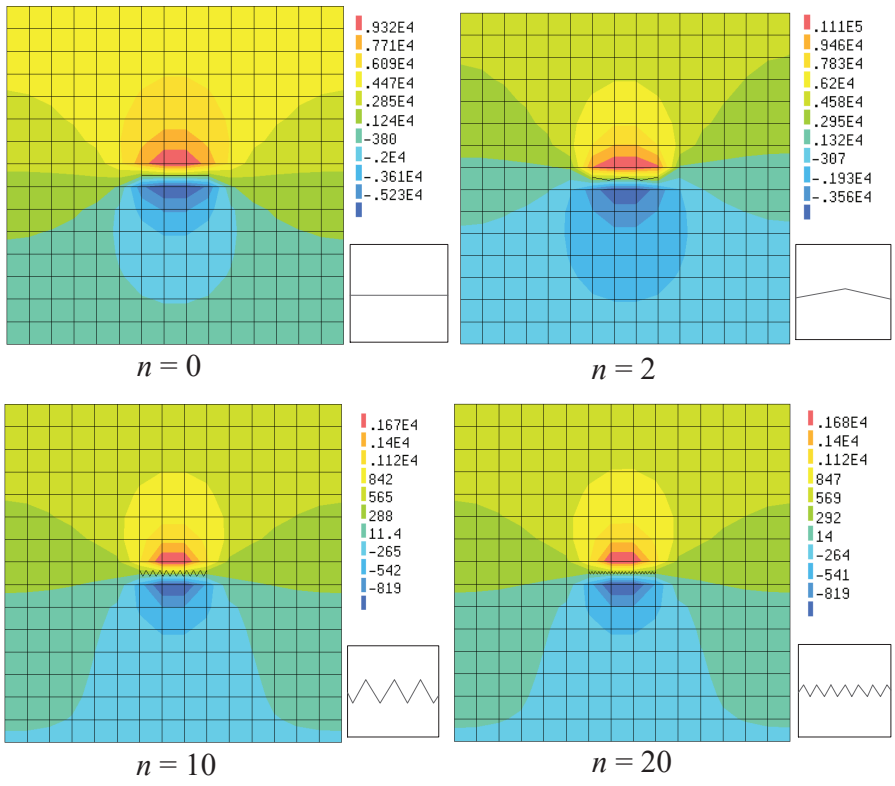

Figure 2: Distributions of excess pressure for different configurations of faults.

4.2. Fluid flow in tetrahedral meshes

To show the applicability of the HNI method to unstructured tetrahedral meshes, a three-dimensional cube $40 \times 40 \times 40$ m^3 is cut by two faults at angles $\alpha_{\mathrm{I}} = -35^\circ$ and $\alpha_{\mathrm{II}} = 55^\circ$. The domain and boundary conditions are shown schematically in Fig. 3. Boundary conditions and material parameters are identical to those in the last case. We adopt an unstructured mesh consisting of 3223 nodes and 16,281 tetrahedral elements.

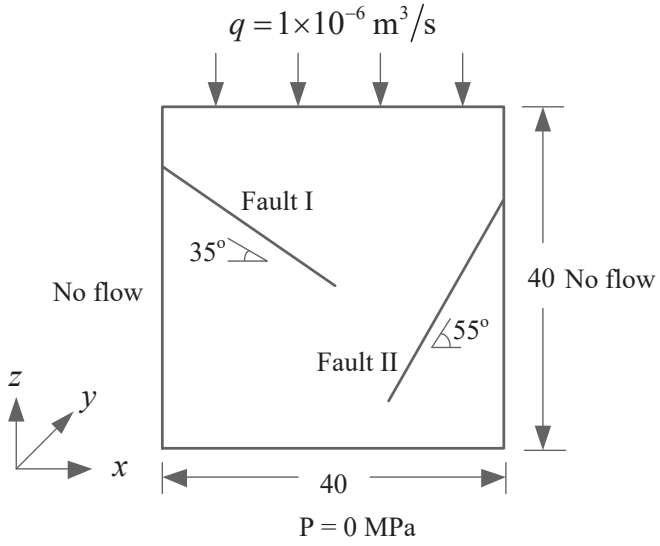

Figure 3: Geometry and boundary conditions for fluid flow in a 3D domain meshed by tetrahedra (Unit: m).

As shown in Fig. 4, we compared the results computed by the HNI method and the integration scheme with element-partitioning. We can see that the distributions of fluid pressure and Darcy velocity for these two methods are almost identical. The maximum pressures are 2.6 MPa for HNI and 2.58 MPa for integration scheme with element-partitioning, respectively. Note that the relative error is less than 1% and the integral result computed by HNI is exact.

The example demonstrates that the HNI method is suitable for unstructured tetrahedral meshes.

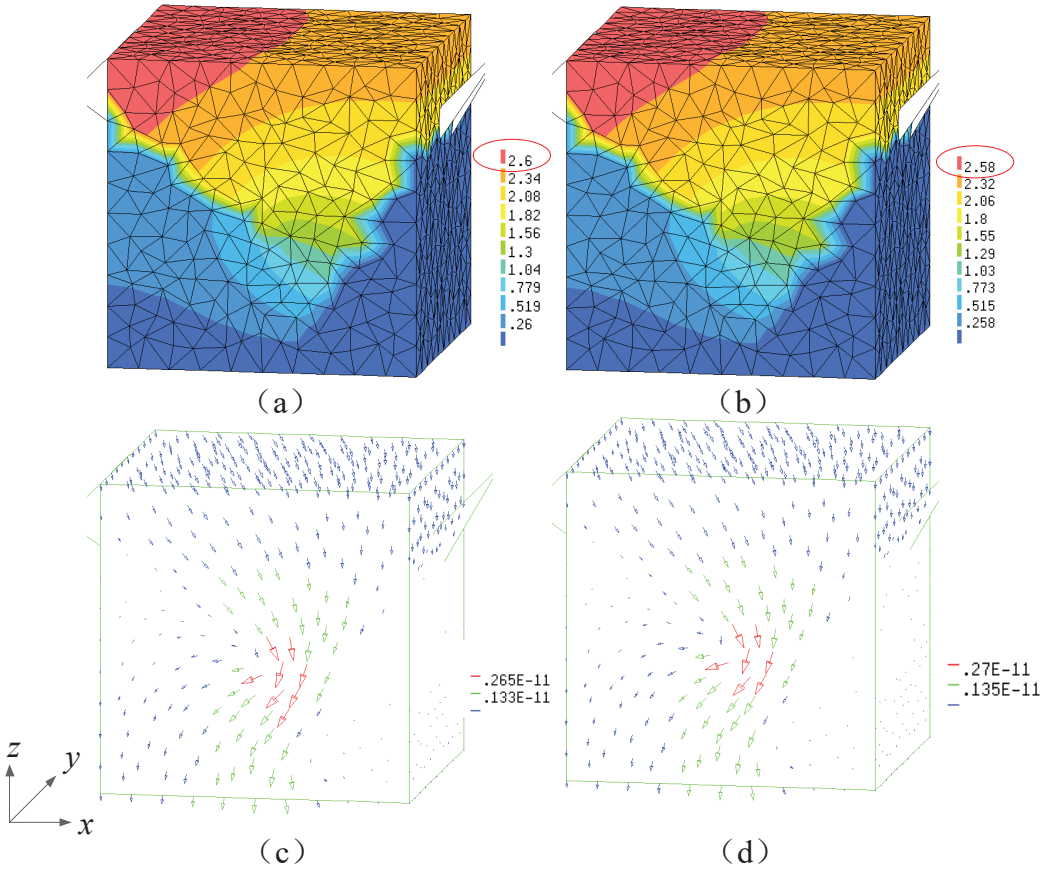

Figure 4: Numerical results for fluid flow problem on tetrahedral meshes. Fluid pressure distribution (MPa) using (a) HNI and (b) element-partitioning. Darcy velocity (m/s) using (c) HNI and (d) element-partitioning.

4.3. Symmetric fluid flow

To further verify the effectiveness of the HNI method for modeling strong and weak discontinuities, as shown in Fig. 5, four symmetric faults (labelled as I, II, III, and IV) with same length 250 m are embedded in a cubic domain with $800 \times 800 \times 800$ m^3. The inclined angle of fault IV is 60°, similar to others.

The boundary conditions and the material parameters are identical to those in the last example but the inflow fluid flux prescribed on the top boundary is $q = 10^{-3}$ m^3/s. The transverse mobility for all faults is $k_n = 0.01k_{rock}$. The longitudinal mobilities are $k_{t,sealing} = 0.01k_{rock}$ for sealing faults and $k_{t,conduit} = 100k_{rock}$ for fluid flow conduits. A structured mesh consisting of regularly shaped hexahedra is adopted and the number of elements is $15\times15\times15 = 3375$. We consider the following three cases: (1) all faults are sealing faults, (2) all faults act as fluid flow conduits, and (3) I and III faults are sealing faults and II and IV faults act as fluid flow conduits. The results are firstly checked in terms of symmetry.

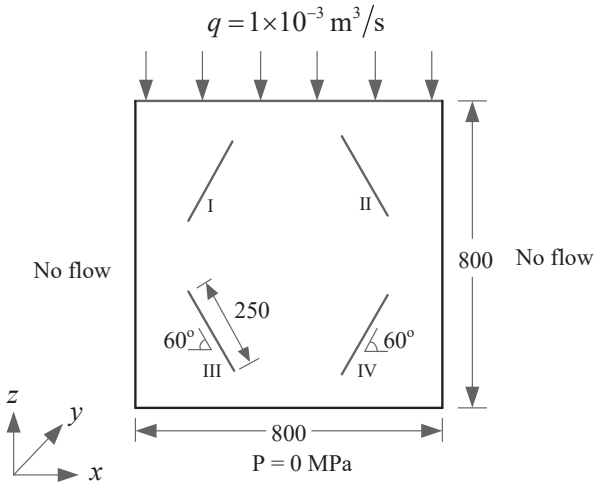

Figure 5: Geometry and boundary conditions for symmetric fluid flow (Unit: m)

Fig. 6 shows the distributions of hydraulic pressure and velocity vectors for different cases. For Case 1, we can see that the hydraulic pressure jumps across the fault, and the high velocities of fluid occur at the boundary regions and the internal region between the faults. For Case 2, the pressure is continuous,

and the maximum fluid velocities are aligned with the longitudinal directions of the faults. The distributions of pressure and velocity are symmetric for both Case 1 and Case 2, which are consistent with the symmetric boundary conditions. For Case 3, pressure jumps occur across the I and III faults, while the maximum fluid velocities are along with the longitudinal directions of the II and IV faults. In summary, the sealing fault works as a barrier to fluid flow resulting in a pressure jump across the fault and the fluid automatically flows along a preferred path with high permeability. The HNI method is suitable to model arbitrary strong discontinuities and planar weak discontinuities in a 3D domain meshed by structured meshes. Further, we compare the computation times for the different cases using the HNI scheme and the integration scheme with element-partitioning to assess the efficiency of HNI (see Table 1). Each value is obtained by averaging the computation times for five trial simulations. We see that the HNI scheme is more efficient for all cases and the approximate speedup, $e = t_{cut}/t_{\text{HNI}}$, is 1.5, where t_{cut} is the computation time using integration scheme with element-partitioning and t_{HNI} is the computation time for the HNI scheme. It should be pointed out that the computational costs for the numerical simulations are only tens of seconds (the calculation for the residuals consume 70% of the whole simulation time) and hence the speedup ratio is not the main focus for fluid flow problems. The main advantage of the HNI over the integration scheme with element-partitioning is the ability to easily handle complex faults, such as the zig-zag fault shown in the last case, without requiring considerable change in the data structure and implementation of new algorithms.

Table 1: Comparison of computation times for different cases using different integration methods

Case	1 (all barriers)		2 (all conduits)		3 (half and half)	
Method	Partitioning	HNI	Partitioning	HNI	Partitioning	HNI
Time	33.7s	18.6 s	32.6 s	22.1 s	31.6 s	22.1s

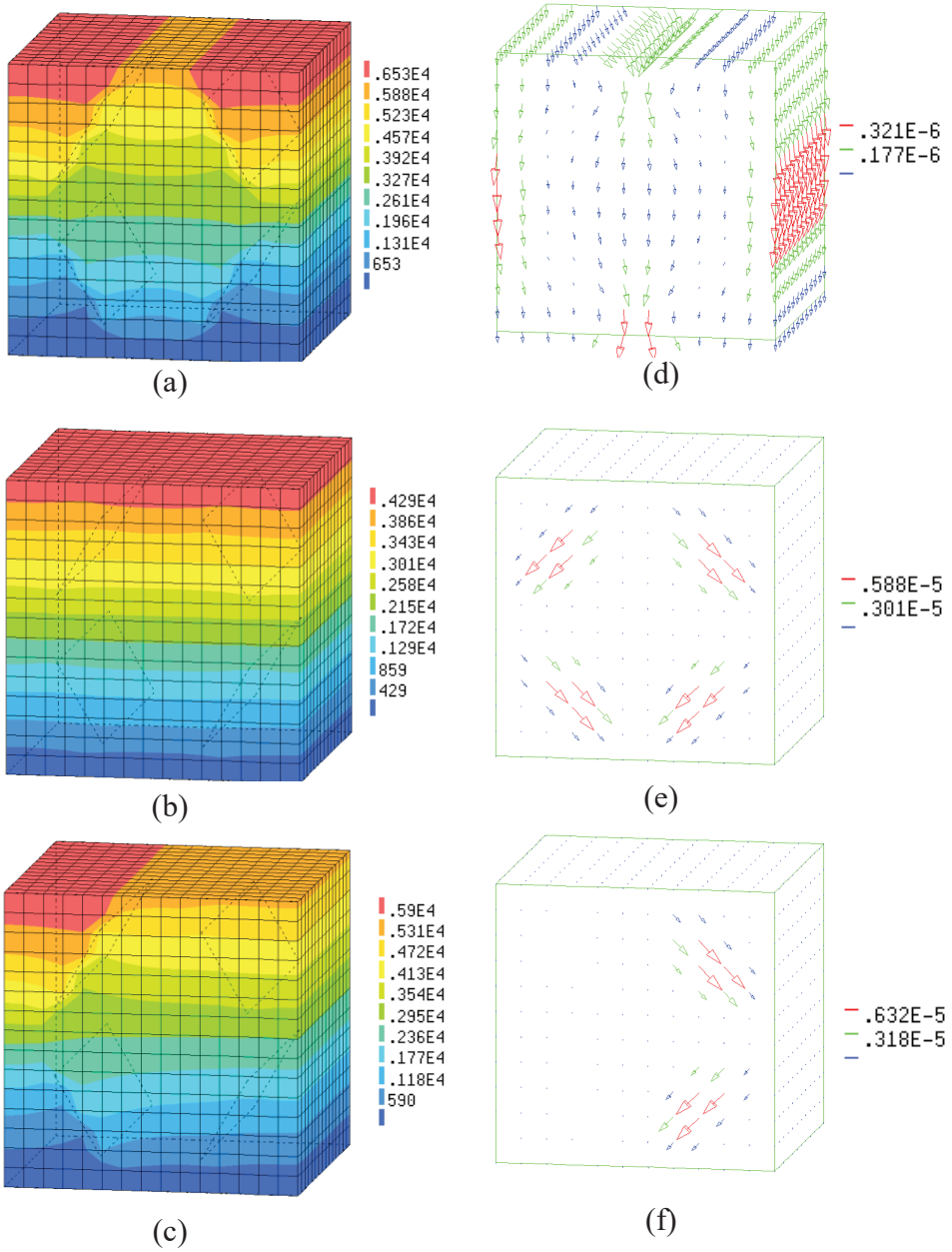

Figure 6: Numerical results for fluid flow problem on structured hexahedral meshes. Fluid pressure distribution (kPa) for (a) Case 1, (b) Case 2 and (c) Case 3. Darcy velocity (m/s) for (d) Case 1, (e) Case 2 and (f) Case 3. Case 1: both faults are sealing faults; Case 2: both faults work as conduits; and Case 3: faults I and III are sealing faults and faults II and IV work as conduits.

4.4. Stress in a 3D domain

In this example, we demonstrate the accuracy of the stress fault model using the HNI scheme. As shown in Fig. 7, a kinked fault consisting of a horizontal branch and a slope branch with angle $\alpha = 60°$, cuts a three-dimensional cube of $500 \times 500 \times 500$ m^3. We set the coordinate system as shown in the figure. A uniform total vertical surface compressive stress is applied on the top surface, i.e. $\sigma_{\mathrm{v}} = 20$ MPa. The vertical displacement of bottom surface is constrained, and the displacements along the x-axis are constrained for the front and back y-z planes. The horizontal compressive stress applied on the lateral boundaries of x-z planes is $\sigma_{\mathrm{H}} = \sigma_{\mathrm{v}} \cdot \nu/(1+\nu)$, where $\nu = 0.25$ is the Poisson's ratio. So the horizontal compressive stress is $\sigma_{\mathrm{H}} \approx 6.67$ MPa. The Young's modulus is $E = 30$ GPa. A structured mesh is adopted, and the total number of elements is 15,625.

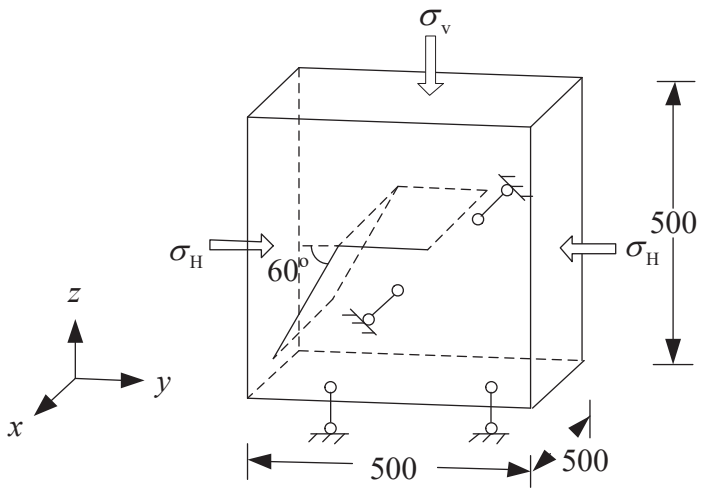

Figure 7: Geometry and boundary conditions for failure analysis in a three-dimensional domain.

For the cohesionless material, the critical friction angle is $\phi = \alpha/2 = 30°$,

which means the fault will slip with a friction angle $\phi < 30°$ and remain stable with a friction angle $\phi > 30°$. The resulting displacement vectors for the fault friction angle $\phi = 32°$ and for the fault friction angle $\phi = 27°$ are shown in Fig. 8a and Fig. 8b, respectively. It can be seen that the slip only occurs for friction angle $\phi = 27°$, as expected. We have compared the results obtained using the HNI scheme and integration scheme with element-partitioning. The results are identical, and the HNI method is approximate 1.5 times faster than the element-partitioning scheme.

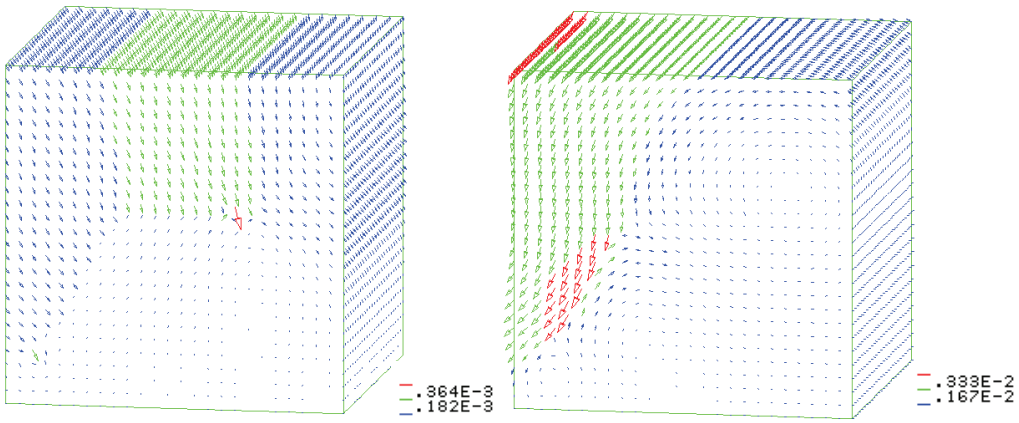

Figure 8: Displacement vectors for different friction angle. no slip along the fault for friction angle $\phi = 32°$ (left); and slip along the fault for friction angle $\phi = 27°$ (right).

4.5. Fully-coupled reservoir-geomechanics

Finally, we demonstrate a fully-coupled reservoir-geomechanical model. As shown in Fig. 9, the slope angle of the sealing fault is 60°. The effective traction applied on the top surface is $\sigma_{\mathrm{v}}^{\prime \mathrm{s}} = 20$ MPa, and the effective traction for the left and right boundaries are $\sigma_{\mathrm{H}}^{\prime \mathrm{s}} = \sigma_{\mathrm{v}}^{\prime \mathrm{s}} \cdot \nu / (1 + \nu)$, where $\nu = 0.25$ is the Poisson's ratio. The solid boundary conditions for the front and back surface are symmetric, and the vertical displacement for the bottom boundary

is constrained. The cube is subjected to a uniform hydraulic pressure, i.e. $p^{\mathrm{f}} = 10$ MPa. There is an injection point located at $(120, 120, 120)$ m, where the pressure piecewise-constantly increases from 10 MPa to 15 MPa . The other material parameters are: Young's modulus for the skeleton $E = 30$ GPa, rock permeability $k_{rock} = 1 \times 10^{-15}$ m^2, friction angle for the fault $\phi = 35°$, cohesion $c = 0$ MPa, fluid viscosity $\mu = 1 \times 10^{-9}$ MPa·s, porosity $n = 0.3$, fluid bulk modulus $K_f = 2$ GPa, and longitudinal and transverse permeability coefficients for the fault $k_n = k_t = 10^{-3} k_{rock}$. The cell size is 20 m, that is 15,625 elements are adopted.

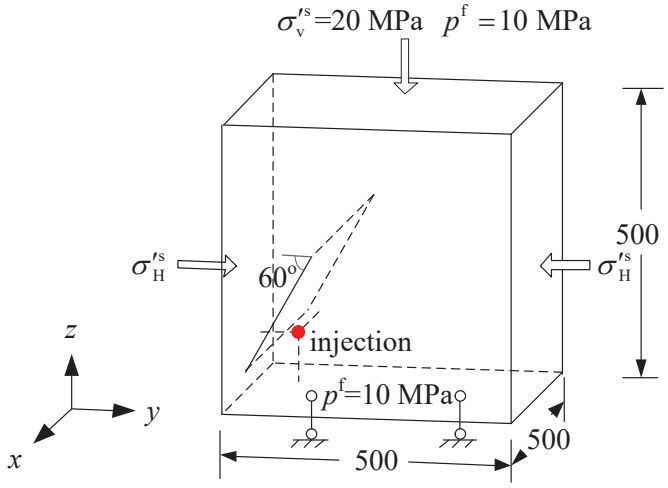

Figure 9: Geometry and boundary conditions for a fully-coupled three-dimensional domain.

Keep in mind that the slope angle for the fault is 60°, which is less than two times of the friction angle $2 \times \phi = 70°$. Therefore, if the pressure of the injection point equals the surrounding hydraulic pressure, the fault will remain stable. Fig. 10 shows the displacement vectors at two specific time instants, i.e., the time instant of applying excess injection pressure and 5 hours after

applying excess injection pressure. The fault will be under a critical state at the moment that the injection pressure changes from 10 MPa into 15 MPa. Then, the fault will slip due to the influence of injection hydraulic pressure. We can see that an apparent failure occurs as shown in Fig. 10b.

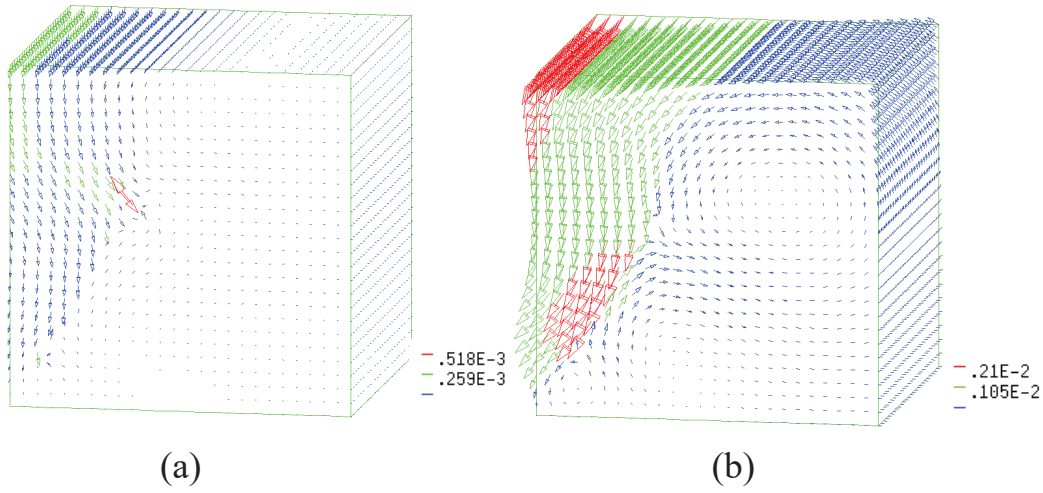

Figure 10: Displacement vectors. (a) at the time instant of applying excess injection pressure; (b) 5 hours after applying excess injection pressure.

5. Conclusions

In this work, we apply a new integration scheme (HNI) for a three-dimensional reservoir-geomechanical model to alleviate the need for element-partitioning in the X-FEM. In the HNI scheme, each cell that is cut by the fault is only decomposed into two simple polyhedra. On using a combination of Stokes's theorem and Euler's homogeneous function theorem, the integration of homogeneous polynomials on each polyhedron is converted to the integration of the same polynomials over the one-dimensional edges of the polyhedron and the integrals results are exact. The HNI method is simple and can be straightforwardly implemented for reservoir-geomechanical models. Structured hexahedral and

unstructured tetrahedral meshes with elements that have planar faces (Jacobian is a constant) are suitable for the HNI method. So it is applicable to most meshes used in practice. An example of a jagged fault showcases the advantages of the HNI method over the integration scheme with element-partitioning that would need complicated algorithms and data structures.

There are hundreds of faults in a real geological domain. If we use the integration scheme with element-partitioning, the coding needs (data structures, sophisticated partitioning algorithms) to readily handle many faults with complex geometries, and the applicability of the three-dimensional reservoir-geomechanical extended finite element model would be limited. The new integration scheme that does not require element-partitioning renders it possible to numerically assess the reactivation of tens to hundreds of faults with complex surface topology in a real geological domain.

Acknowledgements

Funding for this research was partially provided by Princeton University DYNAFLOW research fund.

Reference

J. Sminchak, N. Gupta, C. Byrer, and P. Bergman. Issues related to seismic activity induced by the injection of co_2 in deep saline aquifers. Technical report, National Energy Technology Laboratory, Pittsburgh, PA, and Morgantown, WV (United States), 2001.

W. L. Ellsworth. Injection-induced earthquakes. *Science*, 341(6142):1225942, 2013.

W. Y. Kim. Induced seismicity associated with fluid injection into a deep well in youngstown, ohio. *Journal of Geophysical Research: Solid Earth*, 118(7): 3506–3518, 2013.

J. H. Prévost and N. Sukumar. Faults simulations for three-dimensional reservoir-geomechanical models with the extended finite element method. *Journal of the Mechanics and Physics of Solids*, 86:1–18, 2016.

J. M. Melenk and I. Babuška. The partition of unity finite element method: basic theory and applications. *Computer Methods in Applied Mechanics and Engineering*, 139(1-4):289–314, 1996.

N. Moës, J. Dolbow, and T. Belytschko. A finite element method for crack growth without remeshing. *International Journal for Numerical Methods in Engineering*, 46(1):131–150, 1999.

N. Sukumar, N. Moës, B. Moran, and T. Belytschko. Extended finite element method for three-dimensional crack modelling. *International Journal for Numerical Methods in Engineering*, 48(11):1549–1570, 2000.

N. Sukumar, J. E. Dolbow, and N. Moës. Extended finite element method in computational fracture mechanics: a retrospective examination. *International Journal of Fracture*, 196(1-2):189–206, 2015.

G. Ventura. On the elimination of quadrature subcells for discontinuous functions in the extended finite-element method. *International Journal for Numerical Methods in Engineering*, 66(5):761–795, 2006.

J. B. Lasserre. Integration on a convex polytope. *Proceedings of the American Mathematical Society*, 126(8):2433–2441, 1998.

E. B. Chin, J. B. Lasserre, and N. Sukumar. Modeling crack discontinuities without element-partitioning in the extended finite element method. *International Journal for Numerical Methods in Engineering*, 110(11):1021–1048, 2017.

E. B. Chin, J. B. Lasserre, and N. Sukumar. Numerical integration of homogeneous functions on convex and nonconvex polygons and polyhedra. *Computational Mechanics*, 56(6):967–981, 2015.

L. Jing and O. Stephansson. *Fundamentals of Discrete Element Methods for Rock Engineering: Theory and Applications*, volume 85. Elsevier, 2007.